Computational Investigation of Ripple Dynamics in Biofilms in Flowing Systems

N.G. Cogan[1]

J. Li

S. Fabbri

P. Stoodley

April 9, 2018

Abstract

Biofilms are collections of microorganisms that aggregate using a self-produced matrix of extracellular polymeric substance (EPS). Biofilms are ubiquitous and can be found on almost any solid surface submerged in or exposed to a fluid. It has been broadly demonstrated that many microbial infections in the body, including dental plaque, involve biofilms. While studying experimental models of biofilms relevant to mechanical removal of oral biofilms, distinct ripple patterns have been observed. The rippling provides a place for theoretical models to connect with experiments, validating the models and helping describe the basic physics of the process. Additionally, insight gained from analyzing the physical process of rippling can lead to methods to enhance oral biofilm removal.

In this paper, we describe a multiphase model used to approximate the dynamics of the biofilm removal process. This model treats the biofilm more realistically than simple Newtonian models and has been used to study detachment, deformation, and structural development within a variety of biofilm systems. We show that the the fully nonlinear model provides a better representation of the experimental data than the linear stability analysis. In particular, we show that the full model more accurately reflects the relationship between the apparent wavelength and the external forcing velocities – especially at mid-to-low velocities where the linear theory neglects important interactions. Finally, the model provides a framework where the removal process (presumably governed by highly nonlinear behavior) can be studied.

keywords: Biofilm, multiphase model, Kelvin-Helmholtz

1 Introduction

Biofilms are thin layers of microorganisms in which cells adhere to each other and attach to surfaces. Microbial cells are held together by a matrix consisting of self-produced polymers and other host materials such as proteins and nucleic acids. Free moving, planktonic bacteria initiate a biofilm by attaching to a surface and undergoing a phenotypic switch that upregulates the production of EPS constituents (1). Normally, biofilms are tolerant to antibiotics and disinfectants and employ a multilayered system of defenses that include phenotypic, physiological and physical tolerance (2–4). The focus of this manuscript is on the physical interaction between the biofilm and the bulk flow and is, as such, related to physical protection rather than other mechanisms.

The formation of dental plaque is a common process since the growth and development of oral biofilms are supported by the moist and warm environment in the mouth. Various kinds of bacteria are present in mouth including *Streptococcus mutans* that is the main microorganisms found in oral biofilms (5). As the biofilm matures, changes in bacterial flora lead from health to disease (6–8). There are multiple methods to remove oral biofilms from the surface of teeth including chemical challenges (e.g. mouth rinses) and mechanical methods (e.g. tooth brushing)(9). Compared to chemical dental plaque removal, mechanical methods are more typically effective and usually given priority. Toothbrushing is one of the most commonly used ways to remove dental plaques. Although improving brushing techniques and using electronic toothbrush are helpful in removing plaque build-up, the efficiency of toothbrushing is still not satisfactory since it fails to reach some remote parts of the oral cavity. Hence, other methods including waterpics have been introduced.

To study the process of biofilm removal by exposure to high shear rates, experimental models of oral biofilms were subjected to air and water jets to mimic the effects of physical clearance of biofilms (10). By analyzing high speed video of the dynamics during the erosion process, high velocity ripples were observed and quantified. These ripples had distinct wavelengths that decreased as the forcing velocity increased.

We develop a multiphase model to investigate the removal of the biofilm. For both air and water jets, experiments indicate the formation of distinct ripples which serve as an observable feature with which to compare our theoretical model. In this manuscript we focus on water jets in a fully nonlinear system of equations. Direct numerical simulations provide good agreement with the data and support the hypothesis that the dominant

rippling process is of a Kelvin-Helmholtz type-instability (KHI).

This is an extension of a model focusing on air forcing, but in the linear regime (10). In that model, the biofilm/fluid system was represented as a sharp interface. The external forcing fluid was treated as an Euler flow while the biofilm was treated as a two-phase fluid. Linear analysis showed there was a surface instability (e.g. Kelvin-Helmholtz instability). By matching the peak of the dispersion relation with the wavelength, we were able to compare the wavelength/shear velocity relationship with experimental data. We found fairly good fitting for the relation at higher flow velocities; however, for lower velocities the error between the theoretical result and data become much larger. It is possible the discrepancy was due to a break-down in the assumption (e.g. Euler flow may not be a good approximation for lower velocities) or whether nonlinear affects dominated in this regime.

To explore this, we analyze the multiphase model using direct numerical solution. Rather than treat the problem as a sharp interface between two fluids, we consider the entire domain to consist of a mixture of fluid and network. In the bulk fluid, the network is essentially absent while in the biofilm there is a measurable fraction of biofilm material. This approach has been successfully implemented in a variety of situations previously (11, 12)

We find that the model is consistent with experiments described below. Interestingly, we show that although biofilms in general have been shown to behave as viscoelastic materials, when forced with high velocity bulk fluid, accurate dynamics can be described while neglecting elasticity. This indicates in the experimental regimes studied here viscosity dominates and is enough to quantitatively differentiate observable biofilm structures. This, in turn, provides justification for neglecting elasticity in related applications. The connection between the model and the experiment is demonstrated by the quantitatively accurate comparison between the frequency of waves generated via the KHI theoretically and experimentally.

We note that other studies have considered biofilm ripples as consequences of Kelvin-Helmholtz instabilities (13, 14). In (13), the authors argue that Kinneyia ripple patterns are consequences of KHI. Their results indicate that the ripple wavelength depends primarily on the biofilm depth. However, their analysis differs from this in three primary ways. First the shear rates are substantially different (for mats the flow rates are on the order of 1×10^{-1} m/s while for the experiments described here the flow rates are on the order of $1 \times 10^{1-2}$ m/s). Second, the authors assume a free surface condition for the biofilm interface that simplifies the coupling between the internal and external flow. The free surface condition is likely inaccurate for the high shear rates considered here. Finally, the authors assume that the

biofilm can be treated as a simple viscous material. While drastically simplifying the model equations, there is ample evidence that Stokes equations are not sufficiently robust to model biofilm dynamics (15, 16)

2 Experiment

2.1 Biofilm growth method

Overnight cultures of *S. mutans* UA159 (ATCC 700610) were grown in 2% sucrose-supplemented brain-heart infusion (BHI+S, Sigma-Aldrich). Each overnight culture was diluted in fresh media to an optical density value corresponding to 10^6 cfu/mL for inoculation. *S. mutans* biofilms were grown on autoclaved glass microscope slides (75 mm $\times$ 25 mm, Corning, Sigma-Aldrich). The slides were placed in petri dishes and conditioned with 10 mL of BHI+S and 1% type II porcine gastric mucin (Sigma-Aldrich) (BHI+SM) to simulate salivary proteins and establish a conditioning film. Then the conditioned-slides were inoculated with the *S. mutans* adjusted-overnight culture and grown under static conditions for 72 h at 37 °C and 5% CO^2 with medium replacement every 24 h.

2.2 Micro-channel flow system

Previously we had developed a microfluidic flow channel system (Fabbri et al., 2016b) to study the removal of dental biofilms by high velocity air jets and water spraysspraysprays. Briefly, the flow channel was created by inserting two biofilm colonized glass microscope slides in parallel separated by a distance of 1 mm into a specially fabricated holder. The glass slide enabled high-speed imaging (recorded at between 500 and 8,000 frames per seconds (fps)) with a HSC MotionPro X3 (IDT) equipped with a Sigma 105 mm f/2.8 EX DG Macro lens.

An air piston compressor was used to generate a velocity-controlled forcing jet (ClassicAir 255, Metabo). The average jet velocities (u_0) entering the micro-channel were determined from the volumetric air flow rate (Q_0), measured using a rotometer (FR2000, Key Instruments).

2.3 High-Speed Camera image-processing

Videos were analyzed with the image-processing package Fiji (17). The videos were converted to tiff stacks with each frame in the stack being a different time (T) so that the stack could be represented in XYT co-ordinates.

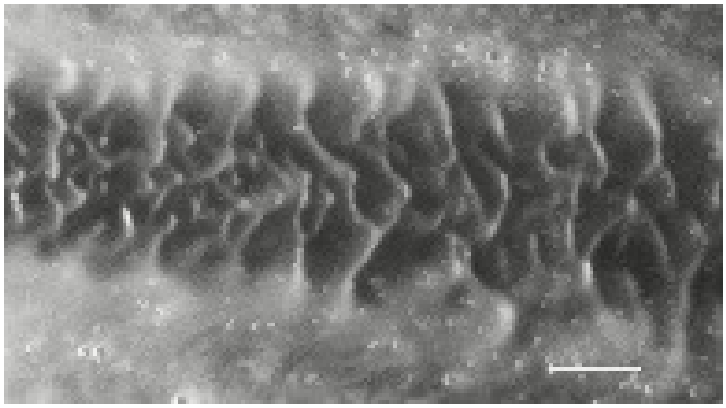

Figure 1: A representative image of the ripples observed. Note that the scale bar is 2 mm.

The ripple's wavelength (λ_R) was measured using the plot profile function. A representative image of the ripples is shown in 1.

The ripple's velocity was measured using the re-slice function which creates a time-trace along a line drawn across the ripple. Using basic image analysis frequencies with the highest identifiable amplitude can be identified – providing a quantitative measure for the wave property (see Figure 2). We use the relationship between the jet velocity and the ripple wavelength measurements as validation data for our theoretical model.

3 Theoretical model

Biofilm removal via external forcing involves the motion and interaction of two materials, i.e. the external flow and the biofilm, which is a typical multiphase fluid dynamics problem. A multiphase model describing the movement and interaction of the biofilm-network and static solvent fluid was developed some time ago (11). Similar models have been used for both Stokes-flow regime and higher Reynolds number systems (12, 19, 20).

In the linear stability analysis performed previously, we treated the problem as a two-fluid problem where the external/forcing was treated as an Euler (infinite Reynolds number) flow and the biofilm was treated as a two-phase mixture (18). Here rather than treating the problem as a sharp interface problem, we consider the diffuse interface problem where the entire domain consists of the multiphase mixture of network and fluid. We initialize the system with biofilm region where the biofilm is present. Outside of

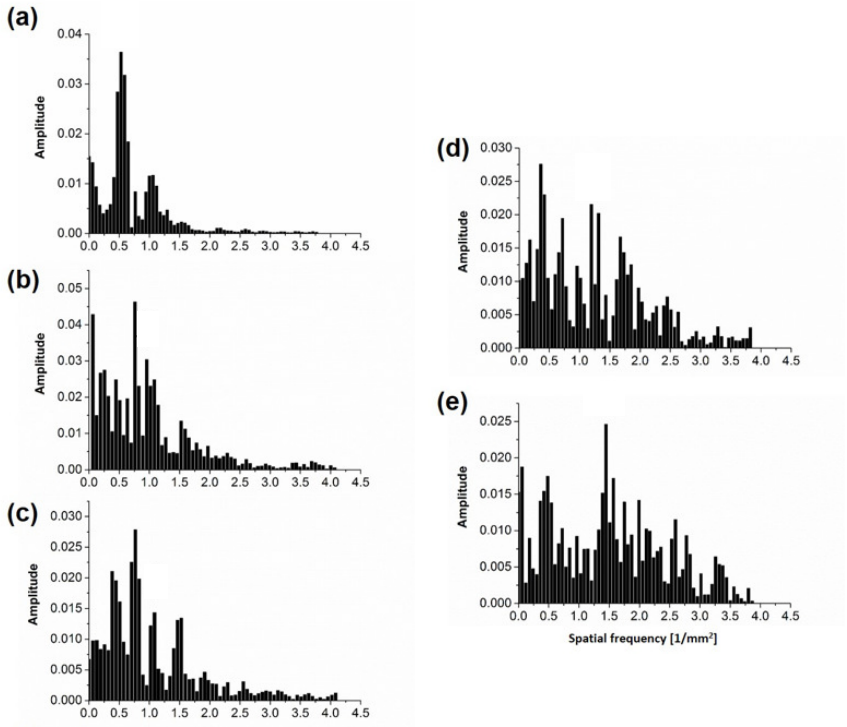

Figure 2: FFT analysis of data collected and analyzed previously (10, 18). *S. mutans* biofilm exposure to fluid jets at (A) 24.6 m/s, (B) 44.9 m/s, (C) 68.1 m/s, (D) 86.5 m/s and (E) 110.1 m/s. Notice that the observed wavelength is less distinct at higher velocities. One hypothesis is that this is due to mixing at higher Reynolds numbers.

that, the biofilm is negligible.

Based on the experimental design, we treat the geometry as a two-dimensional channel. The channel consists of two parallel plates to which biofilms are attached. Forcing fluid enters the domain from the left side of

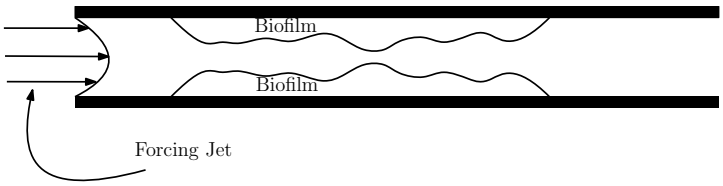

Figure 3: Fluid passes through the channel with biofilm attached. The multiphase description is used to initialize the domain where the entire channel is filled with material, but outside of the biofilm region, the volume fraction of network is zero. Within the indicated biofilm region the network occupies between 5% of the volume.

the channel, passes through the channel and goes out of the channel at the right (see Figure 3).

We assume that there is no biofilm at the entrance and the fluid velocity is well represented by Poiseuille-flow (e.g. parabolic). We define the biofilm via two volume fractions defined as θ_n and θ_f, which represent volume fractions of biofilms and the fluid respectively. If there are no voids or other constituents, the volume fractions sum to one,

$$\theta_n + \theta_f = 1 \tag{1}$$

The phases do not move with the same velocity. Instead, each phases' velocity is governed by a Stokes'-like equation (essentially neglecting inertia). The momentum is described by the balance of three forces that affect the system. The first force is arises from viscosity which is represented as $\eta_* \nabla \cdot (\theta_* (\nabla \vec{U}_* + \nabla \vec{U}_*^T))$. Note that the viscous stress tensor is averaged by the appropriate volume fraction. The second force is the frictional drag from the interaction between two materials (since they are not moving with the same velocity). This force can be described as $h_s \theta_n \theta_f (\vec{U}_n - \vec{U}_f)$ where h_s is a constant coefficient representing the friction drag and $\vec{U}_*$ denotes the velocities of biofilm and fluid. The last force is due to the hydrostatic pressure acting on the two materials proportional to their fraction volumes $-\theta_* \nabla P$. Assuming force balance yields,

$$\frac{\partial \vec{U}_n}{\partial t} = \nabla \cdot (\theta_n \frac{1}{R_n} (\nabla \vec{U}_n + \nabla \vec{U}_n^T)) - h_s \theta_n \theta_f (\vec{U}_n - \vec{U}_f) - \theta_n \nabla P, \tag{2}$$

where R_n is the Reynolds number of biofilms.

The momentum equation for the fluid is similar, but the friction drag acts in the opposite direction, and the hydrostatic pressure force is proportional to the fraction volume of the fluid,

$$\frac{\partial \vec{U}_f}{\partial t} = \nabla \cdot (\theta_f \frac{1}{R_f}(\nabla \vec{U}_f + \nabla \vec{U}_f^T)) + h_s \theta_n \theta_f (\vec{U}_n - \vec{U}_f) - \theta_f \nabla P \qquad (3)$$

where R_f is the Reynolds number for the fluid. Based on the relative length, velocity and viscosities, we estimated that the biofilm has a Reynolds number several orders of magnitude less that that of the fluid (e.g. $R_n = 0.1$ amd $R_f = 200$) (18).

The dynamics of the mass/volume can be modeled by continuity equations,

$$\frac{d\theta_n}{dt} + \nabla \cdot (\theta_n \vec{U}_n) = 0 \qquad (4)$$

$$\frac{d\theta_f}{dt} + \nabla \cdot (\theta_f \vec{U}_f) = 0 \qquad (5)$$

Adding (4), (5) and using (1) yeilds a multiphase incompressible condition

$$\nabla \cdot (\theta_n \vec{U}_n + \theta_f \vec{U}_f) = 0 \qquad (6)$$

The domain is forced from the left, assuming a parabolic velocity profile, with maximum velocity U_0 (since the biofilm is interior to the domain, this applies to the fluid velocity). At the right boundary, biofilm flows out of the domain along with the fluid, so outflow boundary conditions are applied for both velocities and fraction volumes. At the wall, we assume no-slip boundary conditions for both biofilm and fluid velocities. No-flux boundary conditions are assigned to fraction volumes which means neither the biofilm nor the fluid passes through the top or bottom sides.

4 Numerical scheme

For incompressible fluid flow problems, one of the the most popular methods is fractional-step method, or sometimes called projection method, which was first introduced by Chorin and Temam (21). The main difficulty to numerically solve the incompressible fluid equations is that the velocity field and the hydrostatic pressure field are coupled together. The Helmholtz-Hodge decomposition theorem states that any vector function can be decomposed into a divergence-free part plus the gradient of a scalar potential. Based on the theorem, the projection method is able to decouple the velocity and pressure by two steps. In the first step, an intermediate velocity is obtained

by ignoring the incompressibility condition and pressure term. In the second step, the intermediate velocity is projected to the divergence-free field through a pressure correction process.

To apply the projection method to our model, we firstly compute the intermediate velocities $\vec{U}_n^*$ and $\vec{U}_f^*$ from (2) and (3) without pressure terms. As the projection method states, the two intermediate velocities have the following expression,

$$\vec{U}_n^* = \vec{U}_n + \theta_n \Delta t \nabla p \tag{7}$$

$$\vec{U}_f^* = \vec{U}_f + \theta_f \Delta t \nabla p \tag{8}$$

Then multiplying by θ_n and θ_f on both sides of each equation respectively we obtain,

$$\theta_n \vec{U}_n^* = \theta_n \vec{U}_n + \theta_n^2 \Delta t \nabla p \tag{9}$$

$$\theta_f \vec{U}_f^* = \theta_f \vec{U}_f + \theta_f^2 \Delta t \nabla p \tag{10}$$

Adding the above two gives,

$$\theta_n \vec{U}_n^* + \theta_f \vec{U}_f^* = \theta_n \vec{U}_n + \theta_f \vec{U}_f + (\theta_n^2 + \theta_f^2) \Delta t \nabla p \tag{11}$$

then, taking the divergence and making use of the incompressibility condition (5), we end up with a pressure Poisson equation

$$\nabla^2 p = \nabla \cdot \frac{(\theta_n \vec{U}_n^* + \theta_f \vec{U}_f^*)}{(\theta_n^2 + \theta_f^2) \Delta t} \tag{12}$$

The boundary conditions for intermediate velocities are enforced to be the ones of divergence-free velocities. Therefore, homogeneous Neumann boundary conditions for the pressure Poisson equation are required,

$$\hat{n} \cdot \nabla p = 0 \quad on\ \partial\Omega \tag{13}$$

At last, the intermediate velocities are projected to the incompressible (divergence-free) space by a pressure correction

$$U_n^{k+1} = U_n^* - \theta_n \Delta t \nabla P^{k+1} \tag{14}$$

$$U_f^{k+1} = U_f^* - \theta_f \Delta t \nabla P^{k+1} \tag{15}$$

where P^{k+1} is the updated solution of the pressure Poisson equation and U_n^{k+1} and U_f^{k+1} are the updated velocities for the next time step.

The discretization in time is achieved by using Backward Euler method which has the largest stable region. All the spatial derivatives are approximated with second-order central differences on a staggered grid where velocities are evaluated at the center of each edge, while pressure and fraction volume are evaluated at the center of the cell. The advantage of applying the staggered grid to incompressible flows is that *ad hoc* pressure boundary conditions are no longer necessary. In addition, the approximation of spatial derivatives, viscosity, kinetic energy, global conservation of momentum and circulations are preserved (22). However, with the staggered mesh, some of the velocities are not defined on the boundaries and schemes with higher order accuracy are difficult to achieve.

5 Results

Applying the numerical scheme described above to our multiphase model gives the following results. The volume occupied by the biofilm is shown in yellow while the blue denotes volume occupied by the fluid. In Figure 4, we observe the dynamics differ with varying flow velocities at the same time point $T = 50$. To quantitatively measure the wavelength, we applied the Fast Fourier Transformation to numerical simulations (see Figure 5). The wavelength of the numerical result for each velocity is calculated by using the average of frequency accordingly. The comparison with the experimental data are shown in Figure 6. Here, we compare the fitting of the nonlinear analysis (direct numerical simulation) and previous linear stability analysis (23). The nonlinear analysis provides a more realistic wavelength/velocity relation especially in the region with lower velocities.

6 Conclusion

In this paper, we introduced a multiphase model to describe the mixture dynamics during the water pick process. We explored the dynamics of the forced problem, which was previously treated as a two-fluid problem and stability arguments indicated that the observed ripples were likely the result of a Kelvin-Helmholtz instability (10). In addition to being restricted to the linear regime, the previous study also treated the external fluid as an Euler flow. By providing a more robust model, and exploring the dynamics computationally we demonstrate that the previous analysis does describe the development of the waves but the nonlinear simulations provide a better fit to the wave velocity/wavelength relationship observed in experiments.

This provides a theoretical explanation for the experiments designed to study dental plaque removal process. By investigating the fundamental physics, we have some indication that the rippling arises via a Kelvin-Helmholtz instability. Moreover, viscosity dominates the rippling, at least for lower velocity. At higher velocity, neglecting inertial effects reduces agreement between the model and the experimental observations. This provides a path for using the model to develop enhanced removal techniques by optimizing the removal in terms of angle of attack (which was horizontal in this study), varying jet velocity, manipulating the material properties via additions to the forcing jet, etc. Additionally the model can be extended and used to predict drag / detachment / mixing in the biofilm.

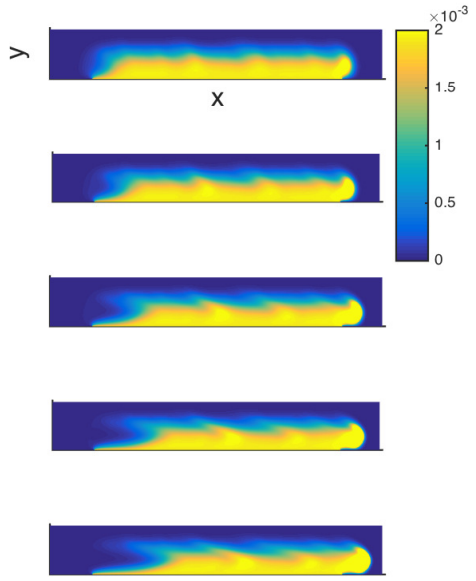

Figure 4: Comparing profiles with increasing background flow velocities, u_0, at time $T = 50$ from top to bottom. The colorbar represents the volume fraction of netowrk. Parameters of the model are: $Re_f = 200$, $Re_n = 0.1$, $hs = 1\frac{Dyn}{cm}$, $\rho_f = 1.23\frac{kg}{cm^3}$, $\mu_f = 0.0018\frac{g}{cm \cdot s}$.

7 Author Contributions

PS designed research and experiments; SF performed experiments and data analysis; JL developed numerical simulations and wrote portions of the manuscript; NC developed model, designed the analysis and wrote portions of the manuscript

8 Acknowledgements

This work was financially funded in part by EPSRC DTP EP/K503130/1 award and in part by Philips Oral Healthcare, Bothell, WA, USA. N.G. Cogan was supported in part by NSF CBET 1510743.

9 References

References

1. David G Davies, Matthew R Parsek, James P Pearson, Barbara H Iglewski, J William Costerton, and E Peter Greenberg. The involvement of cell-to-cell signals in the development of a bacterial biofilm. *Science*, 280(5361):295–298, 1998.

2. N. G. Cogan. Concept in disinfection of bacterial populations. *Mathematical Biosciences*, 245:111–125, 2013.

3. Kelly M Colvin, Vernita D Gordon, Keiji Murakami, Bradley R Borlee, Daniel J Wozniak, Gerard CL Wong, and Matthew R Parsek. The pel polysaccharide can serve a structural and protective role in the biofilm matrix of pseudomonas aeruginosa. *PLoS pathogens*, 7(1):e1001264, 2011.

4. Nicole Billings, Maria Ramirez Millan, Marina Caldara, Roberto Rusconi, Yekaterina Tarasova, Roman Stocker, and Katharina Ribbeck. The extracellular matrix component psl provides fast-acting antibiotic defense in pseudomonas aeruginosa biofilms. *PLoS pathogens*, 9(8):e1003526, 2013.

5. Walter J Loesche. Role of streptococcus mutans in human dental decay. *Microbiological reviews*, 50(4):353, 1986.

6. Susanna Paju and FA Scannapieco. Oral biofilms, periodontitis, and pulmonary infections. *Oral diseases*, 13(6):508–512, 2007.

7. S Filoche, L Wong, and CH Sissons. Oral biofilms: emerging concepts in microbial ecology. *Journal of dental research*, 89(1):8–18, 2010.

8. PD Marsh. Dental diseases–are these examples of ecological catastrophes? *International journal of dental hygiene*, 4(s1):3–10, 2006.

9. Zhou Xuedong. *Dental Caries: Principal and management*. Springer-Verlag Berlin Heidelberg, 1 edition, 2016.

10. Stefania Fabbri, Jian Li, Robert P Howlin, Amir Rmaile, Bart Gottenbos, Marko De Jager, E Michelle Starke, Marcelo Aspiras, Marilyn T Ward, Nicholas G Cogan, et al. Fluid-driven interfacial instabilities and turbulence in bacterial biofilms. *Environmental microbiology*, 19(11):4417–4431, 2017.

11. N. G. Cogan and James P. Keener. The role of the biofilm matrix in structural development. *Mathematical Medicine and Biology*, 21:147–166, 2004.

12. Tianyu Zhang, Nick Cogan, and Qi Wang. Phase field models for biofilms. ii. 2-d numerical simulations of biofilm-flow interaction. *Commun. Comput. Phys*, 4(1):72–101, 2008.

13. Katherine Thomas, Stephan Herminghaus, Hubertus Porada, and Lucas Goehring. Formation of kinneyia via shear-induced instabilities in microbial mats. *Phil. Trans. R. Soc. A*, 371(2004):20120362, 2013.

14. Stephan Herminghaus, Katherine Ruth Thomas, Saeedeh Aliaskarisohi, Hubertus Porada, and Lucas Goehring. Kinneyia: a flow-induced anisotropic fossil pattern from ancient microbial mats. *Frontiers in Materials*, 3:30, 2016.

15. NG Cogan and James P Keener. The role of the biofilm matrix in structural development. *Mathematical medicine and biology: a journal of the IMA*, 21(2):147–166, 2004.

16. Nick G Cogan, John Spencer Gunn, and Daniel J Wozniak. Biofilms and infectious diseases: biology to mathematics and back again. *FEMS microbiology letters*, 322(1):1–7, 2011.

17. J. 1 Schindelin, I. Arganda-Carreras, E. Frise, V. Kaynig, M. Longair, T. Pietzsch, S. Preibisch, C. Rueden, S. Saalfeld, B. Schmid, J. Y. Tinevez, D. J. White, V. Hartenstein, K. Eliceiri, P. Tomancak, and Cardona A. Fiji:. an open-source platform for biological-image analysis. *Nat. Methods*, 9(7):676–82, 2012.

18. Stefania Fabbri, DA Johnston, A Rmaile, B Gottenbos, M De Jager, M Aspiras, EM Starke, MT Ward, and P Stoodley. High-velocity microsprays enhance antimicrobial activity in streptococcus mutans biofilms. *Journal of dental research*, 95(13):1494–1500, 2016.

19. Agnese Seminara, Thomas E Angelini, James N Wilking, Hera Vlamakis, Senan Ebrahim, Roberto Kolter, David A Weitz, and Michael P Brenner. Osmotic spreading of bacillus subtilis biofilms driven by an extracellular matrix. *Proceedings of the National Academy of Sciences*, 109(4):1116–1121, 2012.

20. I Klapper and J Dockery. Role of cohesion in the material description of biofilms. *Physical Review E*, 74(3):031902, 2006.

21. A. J. Chorin. Numerical solution of the Navier-Stokes equations. *Mathematics of Computation*, 22:745–762, 1968.

22. AW Vreman. The projection method for the incompressible navier–stokes equations: The pressure near a no-slip wall. *Journal of Computational Physics*, 263:353–374, 2014.

23. Stefania Fabbri, Jian Li, Robert P Howlin, Amir Rmaile, Bart Gottenbos, Marko De Jager, E Michelle Starke, Marcelo Aspiras, Marilyn T Ward, Nicholas G Cogan, et al. Fluid-driven interfacial instabilities and turbulence in bacterial biofilms. *Environmental microbiology*, 19(11):4417–4431, 2017.

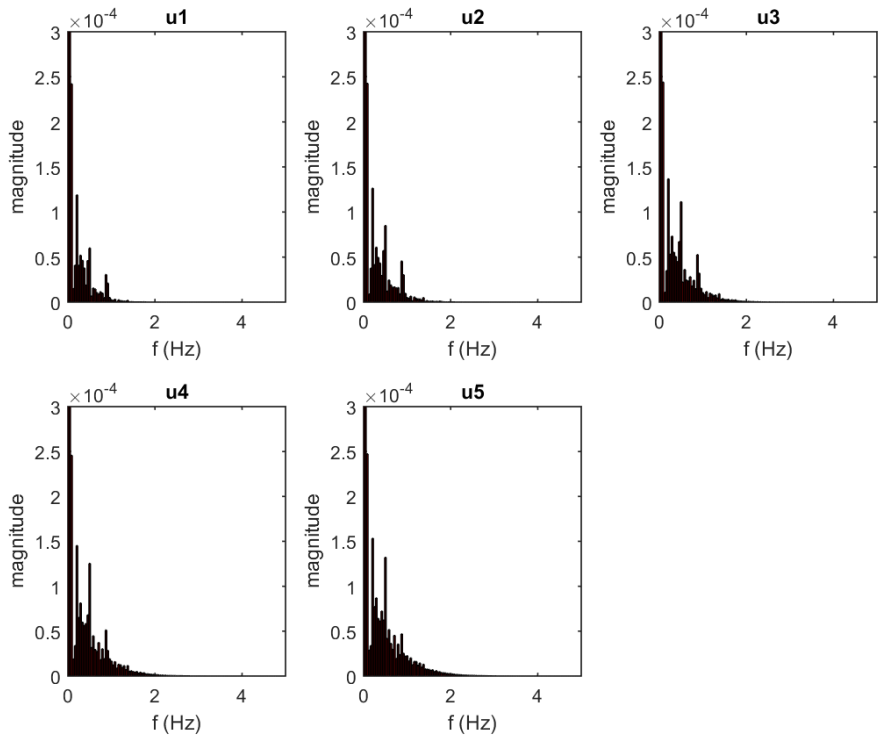

Figure 5: Fast Fourier transformation for spectral analysis, u1=0.246, u2=0.449, u3=0.681, u4=0.855, u1=1.1

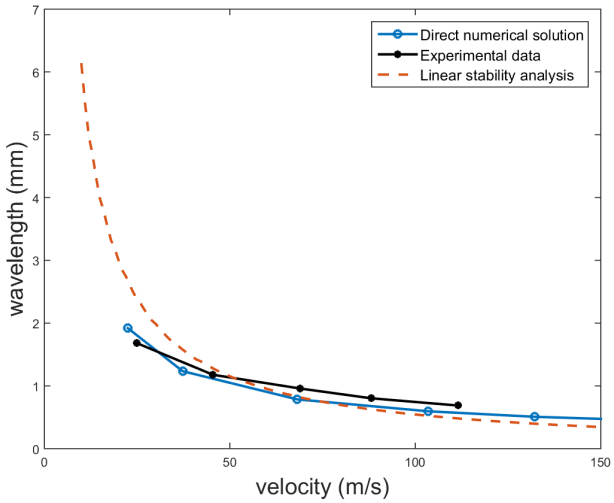

Figure 6: Comparing the wavelength/velocity relation from numerical solutions with experimental data and previous linear stability analysis reported previously (23).